

Journal Pre-proofs

Structural Engineering of Cathodes for Improved Zn-ion Batteries

Jiajia Huang, Yuying Li, Ruikuan Xie, Jianwei Li, Zhihong Tian, Guoliang Chai, Yanwu Zhang, Feili Lai, Guanjie He, Chuntai Liu, Tianxi Liu, Dan J.L. Brett

PII: S2095-4956(20)30670-7
DOI: <https://doi.org/10.1016/j.jechem.2020.09.035>
Reference: JECHEM 1617

To appear in: *Journal of Energy Chemistry*

Received Date: 26 August 2020
Revised Date: 18 September 2020
Accepted Date: 24 September 2020

Please cite this article as: J. Huang, Y. Li, R. Xie, J. Li, Z. Tian, G. Chai, Y. Zhang, F. Lai, G. He, C. Liu, T. Liu, D.J.L. Brett, Structural Engineering of Cathodes for Improved Zn-ion Batteries, *Journal of Energy Chemistry* (2020), doi: <https://doi.org/10.1016/j.jechem.2020.09.035>

This is a PDF file of an article that has undergone enhancements after acceptance, such as the addition of a cover page and metadata, and formatting for readability, but it is not yet the definitive version of record. This version will undergo additional copyediting, typesetting and review before it is published in its final form, but we are providing this version to give early visibility of the article. Please note that, during the production process, errors may be discovered which could affect the content, and all legal disclaimers that apply to the journal pertain.

© 2020 Published by ELSEVIER B.V. and Science Press on behalf of Science Press and Dalian Institute of Chemical Physics, Chinese Academy of Sciences.



Structural Engineering of Cathodes for Improved Zn-ion Batteries

Jiajia Huang^a, Yuying Li^a, Ruikuan Xie^c, Jianwei Li^b, Zhihong Tian^{d,*}, Guoliang Chai^c, Yanwu Zhang^a, Feili Lai^e, Guanjie He^{b,f,*}, Chuntai Liu^d, Tianxi Liu^d and Dan J.L. Brett^b

^a School of Chemical Engineering, Zhengzhou University, Zhengzhou 450001, Henan, China

^b Electrochemical Innovation Lab, Department of Chemical Engineering, University College London, London WC1E 7JE, U.K.

^c State Key Laboratory of Structural Chemistry, Fujian Institute of Research on the Structure of Matter, Chinese Academy of Sciences (CAS), Fuzhou 350002, Fujian, China

^d Key Laboratory of Materials Processing and Mold (Zhengzhou University), Ministry of Education, National Engineering Research Center for Advanced Polymer Processing Technology, Zhengzhou University, Zhengzhou 450002, Henan, China.

^e Department of Chemistry, KU Leuven, Celestijnenlaan 200F, Leuven 3001, Belgium

^f School of Chemistry, University of Lincoln, Joseph Banks Laboratories, Green Lane, Lincoln, LN6 7DL, U.K.

*Corresponding author.

E-mail addresses: g.he@ucl.ac.uk (G. He); zhihong.tian@zzu.edu.cn (Z. Tian).

ABSTRACT

Aqueous zinc-ion batteries (ZIBs) are attracting considerable attention because of their low cost, high safety and abundant anode material resources. However, the major challenge faced by aqueous ZIBs is the lack of stable and high capacity cathode materials due to their complicated reaction mechanism and slow Zn-ion transport kinetics. This study reports a unique 3D ‘flower-like’ zinc cobaltite ($\text{ZnCo}_2\text{O}_{4-x}$) with enriched oxygen vacancies as a new cathode material for aqueous ZIBs. Computational calculations reveal that the presence of oxygen vacancies significantly enhances the electronic conductivity and accelerates Zn^{2+} diffusion by providing enlarged channels. The as-fabricated batteries present an impressive specific capacity of 148.3 mAh g^{-1} at

the current density of 0.05 A g^{-1} , **high energy (2.8 Wh kg^{-1}) and power densities (27.2 W kg^{-1}) based on the whole device**, which outperform most of the reported aqueous ZIBs. Moreover, a flexible solid-state pouch cell was demonstrated, which delivers an extremely stable capacity under bending states. This work demonstrates that the performance of Zn-ion storage can be effectively enhanced by tailoring the atomic structure of cathode materials, guiding the development of low-cost and eco-friendly energy storage materials.

Keywords: Zinc cobaltite; Oxygen vacancies; Aqueous zinc-ion batteries; Flexible solid-state pouch cell

1. Introduction

Stimulated by the growing demands for flexible and wearable electronics, enormous efforts have been focused on the design of flexible rechargeable batteries [1–3]. Lithium-ion batteries have been successfully commercialized, especially in the fields of wearable and portable devices [4–6]. However, lithium-ion batteries have attracted increasing concerns about the limited lithium resources and the high cost [7,8]. Moreover, the flammability and toxicity of the organic electrolytes in lithium-ion batteries raises important safety issues, particularly when they are used in wearable and implantable applications [9–11]. Since aqueous electrolytes exhibit the advantages of lower cost, improved safety and higher ionic conductivity compared with organic electrolytes, it is highly promising to investigate aqueous batteries and further explore their possible application as flexible power resources [12,13]. In this regard, remarkable advancements have been made in aqueous metal-ion (*e.g.* Mg^{2+} , Zn^{2+} , Ca^{2+} , Al^{3+}) batteries [14–17]. Among these aqueous metal-ion systems, Zn-ion batteries (ZIBs) are particularly promising due to the massive merits of low cost (*ca.* $2.3 \text{ \$ kg}^{-1}$), low toxicity, high theoretical capacity (820 mAh g^{-1}) and suitable redox potential (-0.76 V

vs. standard hydrogen electrode) [18,19].

To date, various aqueous Zn-ion batteries have been developed and gained impressive progress. MnO_2 , VO_2 and Prussian blue analogues have been extensively explored and showed considerable specific capacities [20–23]. Besides, recent work has demonstrated that cobalt-based materials acted as the suitable cathodes of aqueous ZIBs with outstanding electrochemical performance, such as $\text{Co}_3\text{O}_4@ \text{NiO}$, $\text{Co}_3\text{O}_4\text{-Co(III)}$ and CoS [24–26]. Compared with binary transition metal oxides, ternary metal oxides display superior electrochemical activities due to their higher electron conductivity and multi-valence states of two transition metals [27]. For instance, Shang *et al.* constructed a Zn battery using self-assembled nanostructured NiCo_2O_4 , showing a specific capacity of $164.25 \text{ mAh g}^{-1}$, and after 1000 discharge-charge cycles, the capacity retention is 63.23% [28]. To further improve the stability of spinel structured materials, other candidates and strategies need to be explored.

Spinel ZnCo_2O_4 materials with bivalent Zn at tetrahedral sites and trivalent Co occupying octahedral sites are widely used for lithium-ion batteries and supercapacitors due to the low cost and superb electrochemical activity [29–31]. Moreover, spinel structured ZnCo_2O_4 is a prospective material for aqueous ZIBs due to the well intercalated Zn-ions in the structure. Recently, Pan and coworkers doped Al in ZnCo_2O_4 and used the material as a cathode for aqueous ZIBs, and $\text{ZnAl}_x\text{Co}_{2-x}\text{O}_4$ material showed capacity of 114 mAh g^{-1} for 100 cycles [32]. Hence, the main issues of ZnCo_2O_4 cathodes are their inferior kinetics and insufficient Zn-ion storage sites. It remains a challenge to inherently improve the kinetics and further induce broader Zn-ion storage channels of ZnCo_2O_4 based cathode materials.

Herein, 3D flower-like ZnCo_2O_4 material was fabricated *via* a simple solvothermal method and abundant oxygen vacancies ($\text{ZnCo}_2\text{O}_{4-x}$) were carefully introduced to boost

its Zn-ion storage performance. This multi-layer 3D ‘microflower’ structure could reduce inherent resistance and improve reaction kinetics, thus providing fast Zn-ion transport channels. Oxygen vacancies not only enhance the concentration of storage sites, but also optimize the electronic conductivity and diffusion channels. As expected, ZnCo₂O₄ materials after introducing the oxygen vacancies (ZnCo₂O_{4-x}) achieve an admirable capacity of 148.3 mAh g⁻¹ at the current density of 0.05 A g⁻¹. Furthermore, a high energy density of 2.8 Wh kg⁻¹, together with a maximum power density of 27.2 W kg⁻¹ based on the mass of whole cell, are achieved by the as-fabricated ZIBs. As a proof-of-concept, a flexible pouch cell ZIB with a solid-state electrolyte was assembled, suggesting stable specific capacity in flatting, folding and bending states.

2. Experimental

2.1. Preparation of ZnCo₂O₄ and ZnCo₂O_{4-x}

The ZnCo₂O₄ was synthesized through a solvothermal method. 0.297 g Zn(NO₃)₂·6H₂O, 0.583 g Co(NO₃)₂·6H₂O, and 0.30 g urea were dissolved in a 40 mL of deionized water (DI water) and ethylene glycol (EG) solvent (V_{DI water}: V_{EG} = 1:1). After being magnetically stirring for 30 min, the resultant solution was loaded into a Teflon-lined stainless-steel autoclave with 50 mL capacity, and maintained in a muffle furnace at 120 °C for 3 h. After reaction, the autoclave was cooled down to room temperature naturally, and the product was harvested, washed several times with DI water and ethanol, respectively, and dried at 80 °C in a vacuum. Later on, the sample was calcined in air at 400 °C for 2 h.

To obtain ZnCo₂O_{4-x}, the as-prepared ZnCo₂O₄ sample was added in a homogeneous solution of 1.5 g NaOH and 40 mL EG. After maintaining at 140 °C for 12 h, the product was taken out, washed with DI water ethanol for several times, and dried in a vacuum oven at 80 °C overnight.

2.2. Electrochemical measurements

To assess the ZIB performance, the cathode was prepared by mixing active material, acetylene black and polyvinylidene fluoride (PVDF) in a weight ratio of 8:1:1 by *N*-methyl-2-pyrrolidone (NMP), and then casting this slurry on carbon paper. After vacuum drying at 80 °C for 12 h, the cathode with $\sim 1.5 \text{ mg cm}^{-2}$ active material was achieved. Zinc foil was used as the counter electrode, glass-fiber membrane as the separator, and 1 M ZnSO_4 as the electrolyte.

The charge/discharge measurements of the cells were tested at different current densities using a LAND battery tester (LAND). Cyclic voltammetry (CV) and electrochemical impedance spectroscopy (EIS) tests were performed by an electrochemical workstation (CHI 660, Chenhua).

2.3. Assembly of the flexible solid-state ZnCo_2O_4 //Zn battery

2.3.1. Pretreatment of carbon cloth

The carbon cloth (CeTech Co., Ltd) was cleaned firstly by acetone and DI water under ultrasonic condition for 20 min. Then, the cleaned carbon cloth was immersed into solution of 65% HNO_3 at 90 °C for 6 h.

2.3.2. Preparation of Polyacrylamide (PAM)/ ZnSO_4 hydrogel electrolyte

10 g acrylamide was dissolved in 10 mL DI water under vigorously stirring at 40 °C for 10 min. Then 10 mg *N,N'*-methylenebisacrylamide and 25 mg potassium persulfate were added into the solution and reacted for 2 h. The obtained mixture solution was poured into a disc mold. In addition, the free-radical polymerization was conducted at 70 °C for 1 h. Finally, the PAM film hydrogel electrolyte was achieved by soaking in solution of 2 M ZnSO_4 overnight.

2.3.3. The preparation of deposited-Zn on carbon cloth electrode

The deposited-Zn on carbon cloth was prepared by a facile electrochemical

deposition method using two-electrode setup. In detail, 6.25 g $\text{ZnSO}_4 \cdot 7\text{H}_2\text{O}$, 6.25 g Na_2SO_4 and 2 g H_3BO_3 were dissolved in 50 mL DI water and used as electrolyte. A two-electrode cell was used with graphite rod as counter electrode and a piece of carbon cloth as work electrode. Electrodeposition was performed with a constant current density of 20 mA cm^{-2} for 20 min at room temperature. The loading mass of Zn is $\sim 9.6 \text{ mg cm}^{-2}$.

2.3.4. Assembly of the flexible solid-state $\text{ZnCo}_2\text{O}_{4-x}/\text{Zn}$ battery

The $\text{ZnCo}_2\text{O}_{4-x}$ electrode was made in the same way as the $\text{ZnCo}_2\text{O}_{4-x}/\text{Zn}$ battery, except for coating on carbon cloth. The flexible solid-state $\text{ZnCo}_2\text{O}_{4-x}/\text{Zn}$ battery was assembled by sandwiching a piece of PAM/ ZnSO_4 hydrogel between $\text{ZnCo}_2\text{O}_{4-x}$ cathode and deposited-Zn on carbon cloth anode, with two Al strips, used as the leads. The battery was assembled in open air conditions and sealed by Al-plastic films by a vacuum sealing system.

2.4. Calculations

The specific capacity (Cm) was calculated from charge/discharge curves according to Eq.(1):

$$Cm = \frac{I \cdot \Delta t}{m} \quad (1)$$

Where the I is the applied current, Δt is the discharging time and m is the mass loading of the active material.

The energy density (E) and power density (P) were calculated from galvanostatic charge/discharge curves according to Eq.(2) and Eq.(3) :

$$E = \frac{I \int_0^{\Delta t} U dt}{m} \quad (2)$$

$$P = \frac{E}{\Delta t} \quad (3)$$

Where I is the discharging current, U is the voltage, Δt is the discharging time and m is the total cell mass (excluding packaging).

2.5. Characterization

The microstructures and compositions of samples were analyzed using scanning electron microscopy (SEM, Zeiss/Auriga Focused ion beam SEM), transmission electron microscopy and high-resolution transmission electron microscopy (TEM and HRTEM, FEI TalosF200S), X-Ray diffraction (XRD, D8 ADVANCE), Laser Raman Spectrometer (Raman, LabRAM HR Evolution), X-ray photoelectron spectroscopy (XPS, VG ESCALAB 220I-XL), Electron paramagnetic resonance (EPR, Bruker EMX_Plus). The specific surface area of the sample was evaluated by Brunauer-Emmett-Teller (BET) method, and the nitrogen (N_2) adsorption-desorption isotherms were measured on an adsorption apparatus (ASAP 2460 Micromeritics instrument) at 77 K. Pore size distribution was estimated from the desorption isotherm by Barrett-Joyner-Halenda (BJH) method.

2.6. Computational method

All the density functional theory (DFT) calculations were performed via the Vienna Ab initio Simulation package (VASP) [33–36], and the projector-augmented plane wave (PAW) pseudopotentials were used for the elements involved [37]. The generalized gradient approximation (GGA) of Perdew, Burke, and Ernzerhof (PBE) was used to treat the exchange-correlation between electrons [38]. The conventional cell of spinel $ZnCo_2O_4$ is shown in Fig. 1. The electron wave function is expanded in plane waves and a cutoff energy of 600 eV is chosen. The Monkhorst-Pack meshes of (9, 9, 9) were adopted for the Brillouin zone (BZ) of the primitive cell [39]. The convergence in the energy and force were set to be 10^{-4} eV and 0.01 eV/Å, respectively.

3. Results and discussion

The fabrication of 3D $\text{ZnCo}_2\text{O}_{4-x}$ flower-like structures with massive oxygen vacancy defects involved a solvothermal and annealing method to form pure ZnCo_2O_4 , followed with a reduction process by using ethylene glycol under alkaline condition to generate oxygen vacancies ($\text{ZnCo}_2\text{O}_{4-x}$). The average bond length between O and neighboring metal atoms is 2.72 Å, thus, the extra space induced by O vacancy (O_v) besides the occupied Zn atoms space will enhance the Zn-ion diffusion, as displayed in Fig. 1.

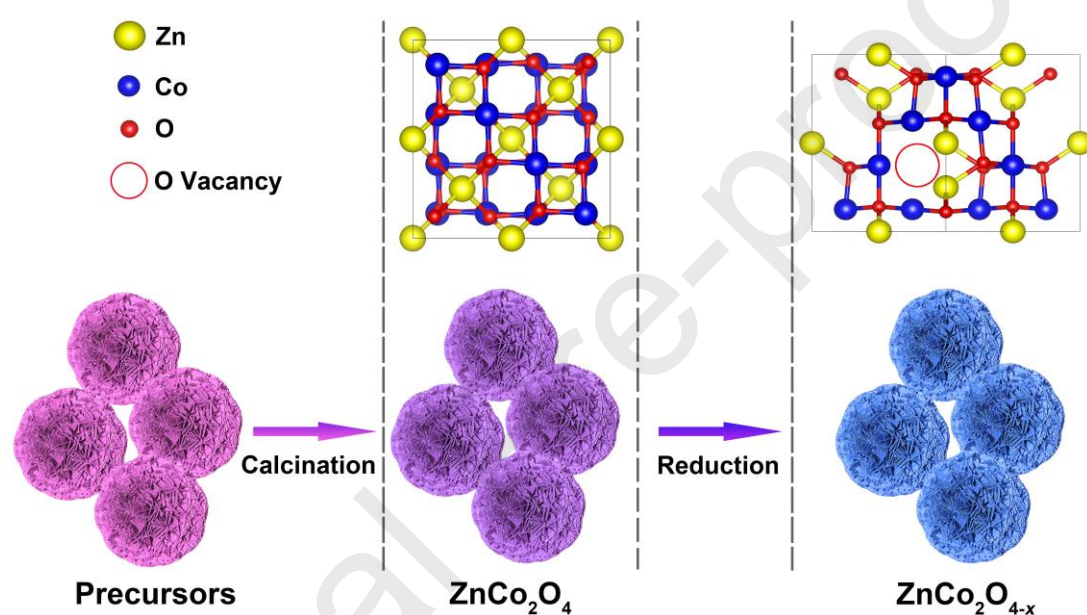


Fig. 1. Schematic illustration of the synthetic process of spinel 3D ZnCo_2O_4 and $\text{ZnCo}_2\text{O}_{4-x}$ flower-like structures.

Fig 2(a) shows the scanning electron microscopy (SEM) images of the micro-structured ZnCo_2O_4 . It is clear that the 3D ZnCo_2O_4 microflowers with a size of $\sim 5 \mu\text{m}$ are dominant. These spherical microflowers consist of nanosheets, and most of these radiate from the center, enhancing the active surface area for Zn-ion adsorption/desorption processes, compared with the large-layered or the nanosheets morphology of 2D materials. Fig. 2(b) demonstrates that the structure of $\text{ZnCo}_2\text{O}_{4-x}$ exhibits great similarities with ZnCo_2O_4 , indicating the reduction treatment did not

change the structure and morphology of 3D microflower. When $\text{ZnCo}_2\text{O}_{4-x}$ is used as a cathode for Zn-ion batteries, this hierarchical 3D microflower structure leads to reduced contact resistance and further fast Zn-ion transport at the electrode/electrolyte interface. Moreover, the ‘petal’ of the microflower shortens the diffusion pathway of Zn-ions and thereby increases the utilization of active materials. Further structural features were elucidated by transmission electron microscopy (TEM). The low-magnification TEM image of an individual $\text{ZnCo}_2\text{O}_{4-x}$ microflower is shown in Fig. 2(c), which is consistent with the SEM observations. Fig. 2(d) reveals that the $\text{ZnCo}_2\text{O}_{4-x}$ nanosheet is composed of a mass of small grains. Furthermore, Fig. 2(e) marks out three clear crystal lattice fringes with interplanar spacings of 0.235, 0.260 and 0.308 nm (from left to right), which correspond to the (222), (311) and (220) lattice planes of ZnCo_2O_4 , respectively. The SAED patterns in the inset of Fig. 2(e) are indexed to the (440), (511), (422), (220), (311) and (400) planes, which indicates a polycrystalline nature of the materials. **The HRTEM image of ZnCo_2O_4 (Fig. S2) indicates the formation of a polycrystalline structure and is similar to the structures of $\text{ZnCo}_2\text{O}_{4-x}$, suggesting the advantage of the mild solvothermal reduction process.** The elemental mapping shown in Fig. 2(f) provides clear information about the elemental distribution within the structures, which further confirms the formation of ZnCo_2O_4 materials.

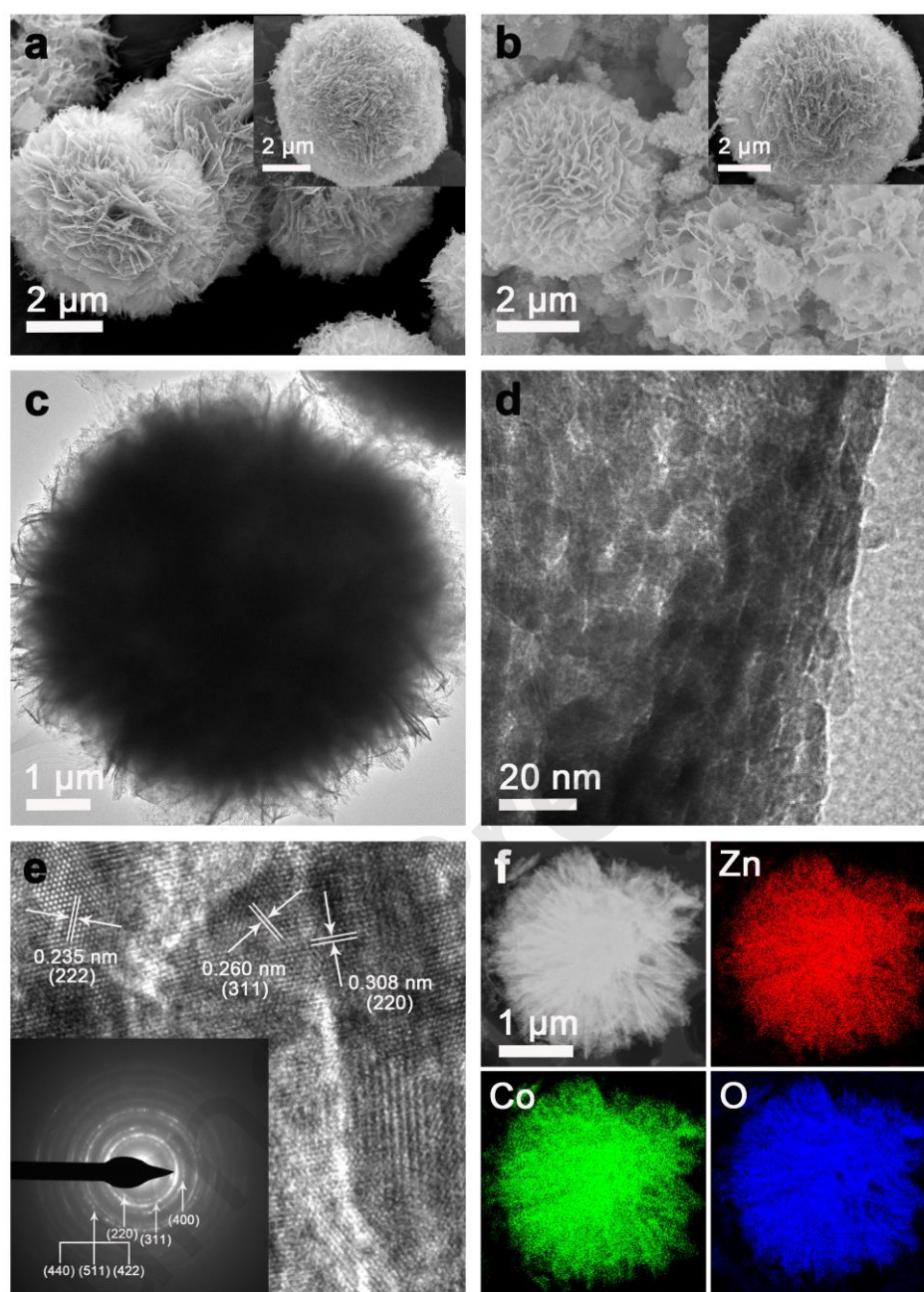


Fig. 2. SEM images of (a) ZnCo_2O_4 , (b) $\text{ZnCo}_2\text{O}_{4-x}$, insets showing a single particle of the materials; (c) low-magnification TEM and (d) high-magnification TEM images of $\text{ZnCo}_2\text{O}_{4-x}$. (e) The corresponding lattice-resolved HRTEM image and SAED pattern of $\text{ZnCo}_2\text{O}_{4-x}$. (f) High angle annular dark-field scanning transmission electron microscope image and corresponding elemental mapping of $\text{ZnCo}_2\text{O}_{4-x}$.

The structural information of the materials was provided by X-ray diffraction (XRD), as shown in Fig. 3(a). The diffraction peaks of ZnCo_2O_4 material are well-indexed to the spinel ZnCo_2O_4 (JCPDF No.23-1390) structure and align with the SAED patterns (Fig. 2e). Meanwhile, $\text{ZnCo}_2\text{O}_{4-x}$ still maintained the original spinel ZnCo_2O_4 structure in spite of the introduction of oxygen defects, suggesting no structural destruction happened during the mild reduction process [40,41]. Raman spectra for the ZnCo_2O_4 and $\text{ZnCo}_2\text{O}_{4-x}$ materials show four peaks centered at 476, 515, 594 and 678 cm^{-1} , attributing to the E_{2g} , $F^{(2)}_{2g}$, $F^{(1)}_{2g}$ and A_{1g} fundamental vibrational models of ZnCo_2O_4 , respectively (Fig. S1). It is found that the peak at 476 cm^{-1} is assigned to the characteristic peak determined by the tetrahedral oxygen and zinc ions of the spinel structure. The peaks at 515, 594, 607 cm^{-1} have been assigned to the characteristic peak of the octahedral oxygen and cobalt ions. Compared with pristine ZnCo_2O_4 , the Raman peak at 594 cm^{-1} for $\text{ZnCo}_2\text{O}_{4-x}$ shifted to a lower wave number due to the decreased concentration of Co^{2+} at octahedral sites on the surface [41,42]. To illustrate the introduction of oxygen vacancies, X-ray photoelectron spectroscopy (XPS) was collected for ZnCo_2O_4 and $\text{ZnCo}_2\text{O}_{4-x}$ materials. The O 1s core level XPS spectra are compared in Fig. 3(b), the peak at 531.2 eV corresponds to the oxygen defects, which belongs to the formation of oxygen vacancy, and another peak at 529.3 eV is typical for metal-oxygen bonds [31,32]. Referring to the evident intensity increase in oxygen defects, it can confirm the introduction of oxygen vacancies for $\text{ZnCo}_2\text{O}_{4-x}$. The normalized Co 2p spectra of both materials are displayed in Fig. 3(c), showing two characteristic Co $2p_{3/2}$ and Co $2p_{1/2}$ peaks. For the $\text{ZnCo}_2\text{O}_{4-x}$ materials, the intensities of the Co^{3+} peaks are dramatically weak while the intensities identified with the enhancement of Co^{2+} peaks, suggesting that Co^{3+} species are reduced to Co^{2+} during the reduction process [34]. As for the peak positions of Zn 2p in $\text{ZnCo}_2\text{O}_{4-x}$ materials,

no change in ZnCo_2O_4 peaks indicates they have the same valence state as Zn^{2+} (Fig. S3). XPS survey spectrum strongly suggests that the reduction treatment did not destroy the structure and the Zn:Co ratios (Fig. S4a). Energy dispersive X-ray spectroscopy (EDX) provide additional support for this conclusion (Fig. S4b). Electron paramagnetic resonance (EPR) spectroscopy was also performed to verify the magnetically active sites of $\text{ZnCo}_2\text{O}_{4-x}$ crystalline structures. As shown in Fig. 3(d), at a g value of 2.075, a strong signal peak attributed to Co^{2+} is noticed for the $\text{ZnCo}_2\text{O}_{4-x}$ materials, revealing the generation of Co^{2+} species during the reduction treatment, which is consistent with the XPS results [40].

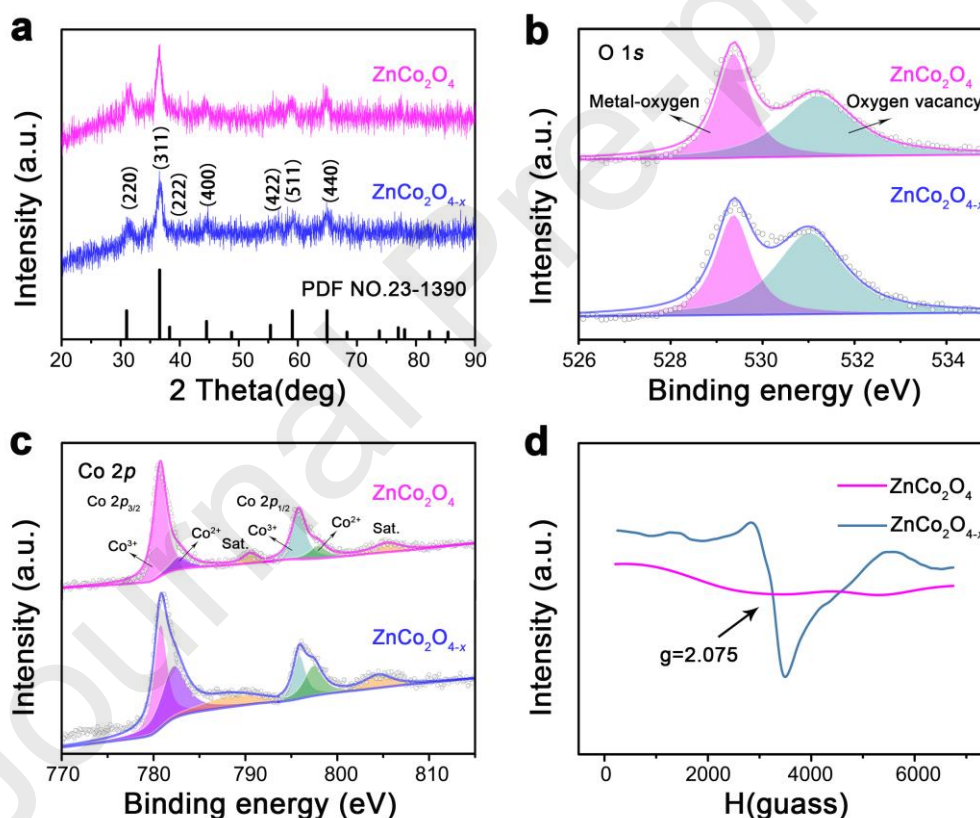


Fig. 3. (a) XRD patterns, (b) O 1s XPS, (c) Co 2p XPS, (d) EPR spectra of ZnCo_2O_4 and $\text{ZnCo}_2\text{O}_{4-x}$ materials, respectively.

The electrochemical performances of 3D ZnCo_2O_4 and $\text{ZnCo}_2\text{O}_{4-x}$ flower-like nanostructures as cathodes for ZIBs were investigated in assembled CR2032-type coin

cells. Fig. S5 compares the cyclic voltammetry (CV) curves of the ZnCo_2O_4 and $\text{ZnCo}_2\text{O}_{4-x}$ electrodes at the scan rate of 1 mV s^{-1} in the potential range of $0.2\sim 1.9 \text{ V vs. Zn}^{2+}/\text{Zn}$, from which two distinct peaks are observed for both curves. It is noted that the $\text{ZnCo}_2\text{O}_{4-x}$ materials exhibit larger current densities than that of the ZnCo_2O_4 ones, demonstrating the positive influence of the introduction of oxygen vacancies. To further reveal the electrochemical kinetics of the $\text{ZnCo}_2\text{O}_{4-x}$ electrodes, the linear relationship between the square root of the scan rate ($v^{1/2}$) and the cathodic peak current densities (i) at different scan rates is presented in Fig. 4(a), indicating that the redox reaction at the $\text{ZnCo}_2\text{O}_{4-x}$ electrode is a diffusion-controlled process [43,44]. Fig. 4(b) shows the charge/discharge curves of the ZnCo_2O_4 (the theoretical capacity $\approx 216 \text{ mAh g}^{-1}$) and $\text{ZnCo}_2\text{O}_{4-x}$ electrodes at the current density of 0.05 A g^{-1} within $0.2\sim 1.75 \text{ V}$. Compared to ZnCo_2O_4 electrodes (89.7 mAh g^{-1}), the capacity of $\text{ZnCo}_2\text{O}_{4-x}$ electrodes has increased by more than 65 %, which reaches up to 148.8 mAh g^{-1} . **Such high specific capacity of $\text{ZnCo}_2\text{O}_{4-x}$ electrode exceeds other ZIB cathodes reported recently, such as $\text{Zn}(\text{Fe}(\text{CN})_6)_2$ (65.4 mAh g^{-1}) [45], Ni_3S_2 (148 mAh g^{-1}) [46], NiHCF (76.2 mAh g^{-1}) [47], $\text{ZnHCF}@\text{MnO}_2@\text{Ni foil}$ (118 mAh g^{-1}) [48], $\text{Na}_3\text{V}_2(\text{PO}_4)_3/\text{C}$ (92 mAh g^{-1}) [49], CuHCF (53 mAh g^{-1}) [50], revealing the boosted capacity of this material after introducing oxygen defects (Table S1).** Fig. 4(c) and Fig. S6 record the rate performance of two materials for 35 continuous cycles; $\text{ZnCo}_2\text{O}_{4-x}$ materials produce a higher capacity at any discharge current densities. Even at a high current density of 2 A g^{-1} , the capacity of $\text{ZnCo}_2\text{O}_{4-x}$ electrodes still retains 47.5 mAh g^{-1} . After cycling back to 0.05 A g^{-1} , an average discharge capacity recovers to 148.3 mAh g^{-1} , indicating its remarkable rate capability and stability. Additionally, it is noteworthy that after the initial several cycles, the Coulombic efficiency of $\text{ZnCo}_2\text{O}_{4-x}$ electrodes increases to approximately 100%, indicating excellent reversibility during charge/discharge

processes. This superior capacity is based on the following Faradaic redox reaction between ZnCo_2O_4 cathodes and Zn anodes with mild electrolyte [51–54]:

Cathode reaction:



Anode reaction:



Full cell reaction:

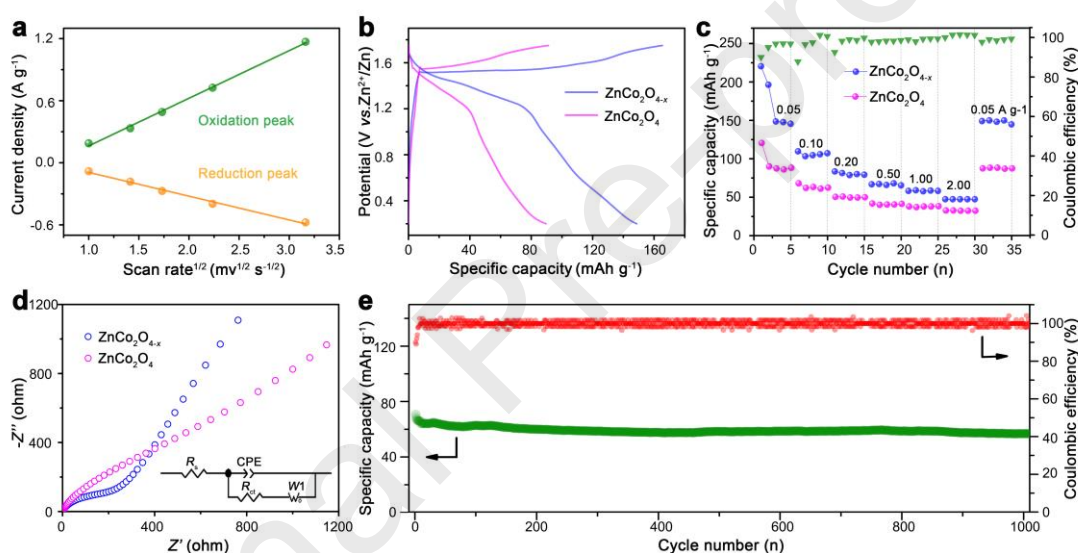


Fig. 4. (a) The relationship between the redox peak currents and the square roots of the scan rates for $\text{ZnCo}_2\text{O}_{4-x}$ materials from CV curves, (b) charge/discharge curves at the current density of 0.05 A g^{-1} , (c) rate performances, (d) nyquist plots of the ZnCo_2O_4 and $\text{ZnCo}_2\text{O}_{4-x}$ materials, inset showing the equivalent circuit to simulate the resistance, respectively, (e) cycling performance of the $\text{ZnCo}_2\text{O}_{4-x}$ materials over 1000 cycles.

The improved electrochemical performance of the $\text{ZnCo}_2\text{O}_{4-x}$ electrode was further demonstrated by electrochemical impedance spectroscopy (EIS). The corresponding equivalent circuit and fitting results for the ZnCo_2O_4 and $\text{ZnCo}_2\text{O}_{4-x}$ materials are

depicted in Fig. 4(d) [52]. The diagram is composed of four electronic components, where R_s is the purely ohmic resistance, the CPE stands for the constant phase element, the R_{ct} is the charge transfer resistance, and the W_1 represents the Warburg impedance. The plot for $ZnCo_2O_{4-x}$ electrodes shows a smaller semicircle in the high-frequency area, which suggests that it has a much smaller charge-transfer resistance ($\approx 160 \Omega$) than the $ZnCo_2O_4$ electrodes ($\approx 272 \Omega$), indicating the substantially enhanced electronic conductivity due to the introduction of the oxygen defects. Furthermore, the Brunauer–Emmett–Teller (BET) surface area of $ZnCo_2O_{4-x}$ ($100.6 \text{ m}^2 \text{ g}^{-1}$) is larger than that of $ZnCo_2O_4$ materials ($77.3 \text{ m}^2 \text{ g}^{-1}$) (Fig. S7), demonstrating that the $ZnCo_2O_{4-x}$ material has the higher surface reactivity which contributed to faster reaction kinetics. **The as-fabricated Zn-ion battery reveals both remarkably high-power density of 27.2 W kg^{-1} and energy density of 2.8 Wh kg^{-1} based on the mass of whole cell (excluding packaging).** Impressively, the battery exhibits a high capacity retention of 84% and Coulombic Efficiency about 100% after 1000 cycles at 0.5 A g^{-1} (Fig. 4e) with highly similar charge/discharge curves during long-term examination (Fig. S8).

To reveal the electronic properties of the materials, the band structure and density of states are calculated *via* DFT method. As shown in Fig. 5(a), the band gap of pristine $ZnCo_2O_4$ is 0.91 eV which is too large since better electron conductivity for energy storage materials is encouraged. The density of states indicates that the valence band maximum (VBM) and the conduction band minimum (CBM) mostly originate from Co-3d and O-2p states (Fig. 5b). Zn-3d states locate deeply under Fermi energy level and contribute nearly nothing to VBM and CBM. Thus, introducing O_v is a promising way to tune the energy gap. Then, one O atom from the primitive cell was removed and the band structure and density of states are shown in Fig. 5(c and d), respectively. O_v , a typical n-type defect, can induce donor state above VBM as marked out with a red

arrow in Fig. 5c and the band gap is decreased to 0.76 eV. The density of states, as shown in Fig. 5d, indicates that the composition of VBM and CBM remains unchanged but extra states arise around them which is consistent with the analysis above. If another O atom is removed, more donor states will be introduced and the band gap will be further decreased to 0.5 V (Fig. S9) and better conductivity can be expected. Furthermore, the average bonding length between O and neighboring metal atoms is about 1.95 Å. Thus, the diameter of the extra channel caused by O_v is about 3.9 Å (initial diameter: 1.95 Å), which will make enough space for Zn-ion diffusion as shown in Fig. 1. **Therefore, it is found that the O_v would promote charge conductivity and further enhance electrochemical kinetic and Zn storage ability [52,54–55].**

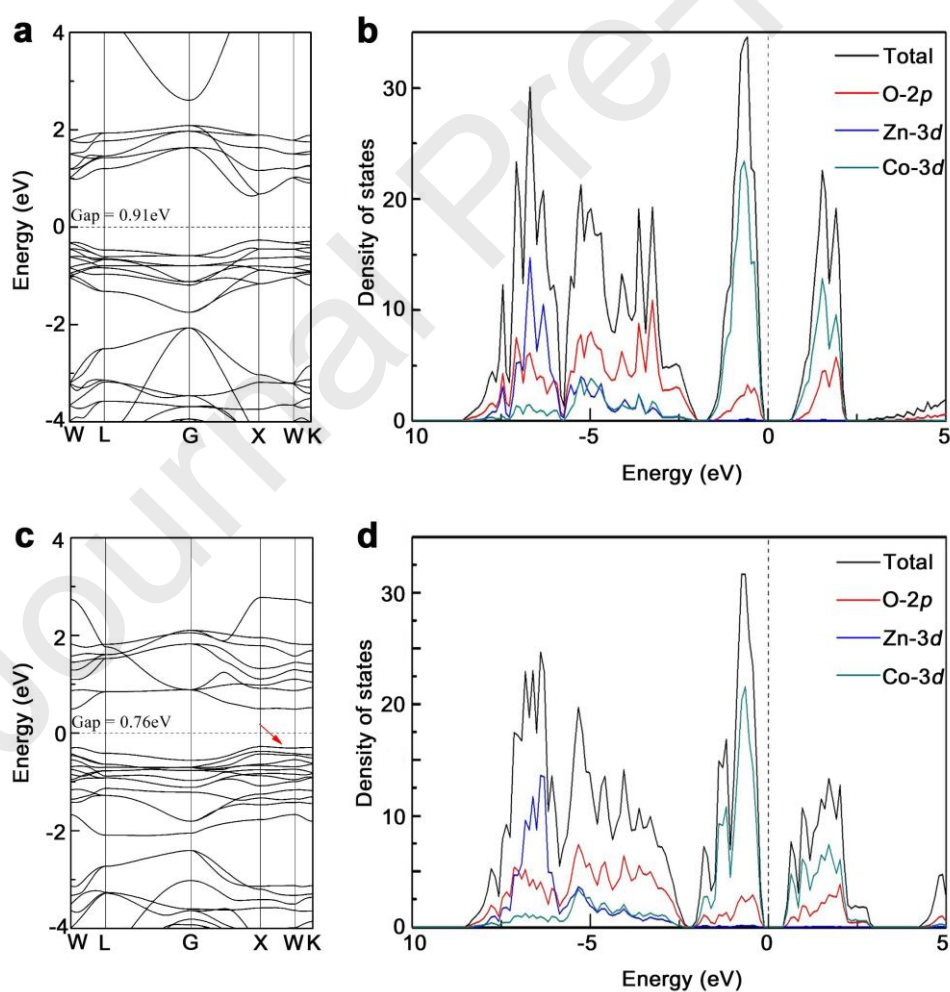


Fig. 5. (a) Band structure, (b) density of states of pristine ZnCo_2O_4 materials; (c) band structure, (d) density of states of ZnCo_2O_4 materials with one O_v

To determine the potential applications of as-designed batteries in a real application under different working conditions, flexible solid-state $\text{ZnCo}_2\text{O}_{4-x}/\text{Zn}$ rechargeable batteries were assembled. To realize the outstanding electrochemical performance of the aqueous $\text{ZnCo}_2\text{O}_{4-x}/\text{Zn}$ batteries in pouch cells, the flexible solid-state rechargeable $\text{ZnCo}_2\text{O}_{4-x}/\text{Zn}$ batteries were assembled with a sandwich configuration. As illustrated in Fig. 6(a), the flexible solid-state $\text{ZnCo}_2\text{O}_{4-x}/\text{Zn}$ batteries were assembled by coating a flexible Zn-deposited anode and $\text{ZnCo}_2\text{O}_{4-x}$ cathode on each side of the polyacrylamide (PAM)/ ZnSO_4 hydrogel electrolyte, and then sealed by Al-plastic films. The Zn-deposited anode displays a uniform nanosheet structure and carbon cloth has a porous structure as shown in Fig. S10, which is conducive to immersing of the electrolyte and Zn-ion transfer. **Fig. S11 shows that the hydrogel electrolyte is about 0.6 mm thick and exhibits a low resistance.** It is noted that the fabrication of the flexible solid-state batteries is facile and safe, lending the technology to ease of scaling up. Besides, because of the flexibility of the electrodes and the hydrogel electrolyte, the solid-state batteries reveal a remarkable flexibility to sustain multiple deformations including folding and bending. Fig. 6(b) depicts the CV curve at 5 mV s^{-1} , which shows similar shapes with those tested in aqueous electrolyte, demonstrating that the outstanding Zn^{2+} intercalation/deintercalation behavior of $\text{ZnCo}_2\text{O}_{4-x}$ cathode is also applicable in solid-state electrolyte. **The EIS of the flexible solid-state $\text{ZnCo}_2\text{O}_{4-x}/\text{Zn}$ battery is displayed in Fig. S12.** The performance of the flexible solid-state $\text{ZnCo}_2\text{O}_{4-x}/\text{Zn}$ batteries still present an excellent specific capacity of 64.5 mAh g^{-1} at 0.5 A g^{-1} based on the total mass of $\text{ZnCo}_2\text{O}_{4-x}$ materials on the cathodes. Fig. 6(c) further displays the charge/discharge curves of the batteries under

flattening, folding in 90° , folding in 180° and bending conditions. It is important to note that the difference between these four curves is negligible. Moreover, as shown in Fig. 6(d), after the battery recovered from bending to the flat state after 40 cycles, the specific capacity of 62.8 mAh g^{-1} was retained, proving its feasibility in flexible electronics. To verify the practical viability of the flexible solid-state $\text{ZnCo}_2\text{O}_{4-x}/\text{Zn}$ batteries, two $\text{ZnCo}_2\text{O}_{4-x}/\text{Zn}$ batteries were connected in series. They can light up a green light-emitting diode (LED) under flattening, folding and bending states (Fig. 6e and Fig. S13), emphasizing the flexibility of these solid-state $\text{ZnCo}_2\text{O}_{4-x}/\text{Zn}$ batteries. In addition, a humidity thermometer is also powered by two flexible solid-state $\text{ZnCo}_2\text{O}_{4-x}/\text{Zn}$ batteries in tandem (Fig. S14), further showing the practical application of the $\text{ZnCo}_2\text{O}_{4-x}/\text{Zn}$ battery in flexible and wearable energy storage devices.

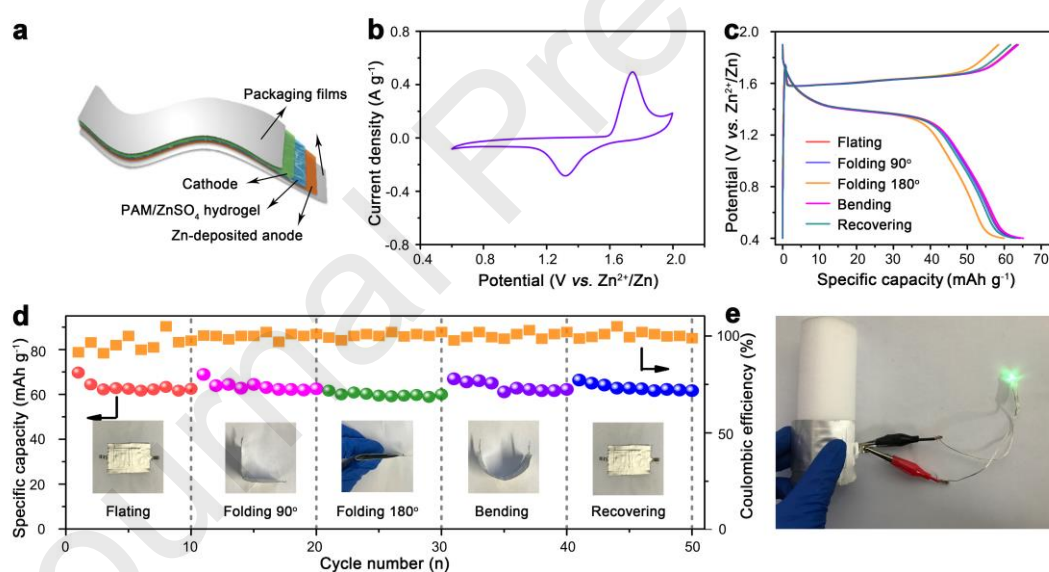


Fig. 6. (a) Schematic diagram of the flexible solid-state $\text{ZnCo}_2\text{O}_{4-x}/\text{Zn}$ battery, (b) CV curves at the scan rate of 5 mV s^{-1} for the flexible solid-state $\text{ZnCo}_2\text{O}_{4-x}/\text{Zn}$ battery, (c) charge/discharge curves at 0.5 A g^{-1} , (d) cycling performance at 0.5 A g^{-1} under different mechanical deformations of the flexible solid-state $\text{ZnCo}_2\text{O}_{4-x}/\text{Zn}$ battery. (e) Photographs of an LED light powered by two flexible solid-state $\text{ZnCo}_2\text{O}_{4-x}/\text{Zn}$

batteries in tandem.

4. Conclusions

In summary, 3D ZnCo₂O₄ flower-like nanostructures with carefully induced oxygen vacancies forming ZnCo₂O_{4-x} have been synthesized successfully and used as cathode materials for aqueous ZIBs. This unique structure is expected to not only enhance the active surface area, but also improve the Zn-ion diffusion channels and electronic transfer. These important features make ZnCo₂O_{4-x} deliver a capacity of 148.3 mAh g⁻¹ and good long-term stability with capacity retention of more than 84% after 1000 cycles. Moreover, the flexible solid-state pouch ZnCo₂O_{4-x}//Zn batteries are assembled, achieving a stable energy storage ability under different mechanical deformations. The atomic structural engineering strategy presented in this work is expected to improve the electrochemical performances of other electrode materials in aqueous electrolyte. Additionally, this work reveals great potentials for ZIBs as flexible and wearable rechargeable devices.

Acknowledgements

This work was supported by the National Natural Science Foundation of China (No. 51873198, 51503184 and 21703248), the Strategic Priority Research Program of the Chinese Academy of Sciences (Grant No. XDB20000000), the Engineering and Physical Sciences Research Council (EPSRC, EP/R023581/1) and the STFC Batteries Network (ST/R006873/1).

References

- [1] Z. Wu, Y. Wang, X. Liu, C. Lv, Y. Li, D. Wei, Z. Liu, *Adv. Mater.* 31 (2019) 1–25.
- [2] L. Zeng, L. Qiu, H.M. Cheng, *Energy Storage Mater.* 23 (2019) 434–438.
- [3] C. Wang, K. Xia, H. Wang, X. Liang, Z. Yin, Y. Zhang, *Adv. Mater.* 31 (2019) 1–37.
- [4] H. Tabassum, R. Zou, A. Mahmood, Z. Liang, Q. Wang, H. Zhang, S. Gao, C. Qu, W. Guo, S. Guo, *Adv. Mater.* 30 (2018) 1–7.

- [5] R. Zou, M. Xu, S.A. He, X. Han, R. Lin, Z. Cui, G. He, D.J.L. Brett, Z.X. Guo, J. Hu, I.P. Parkin, *J. Mater. Chem. A* 6 (2018) 19853–19862.
- [6] Y. Lu, X. Hou, L. Miao, L. Li, R. Shi, L. Liu, J. Chen, *Angew. Chemie - Int. Ed.* 58 (2019) 7020–7024.
- [7] H. Zhang, I. Hasa, S. Passerini, *Adv. Energy Mater.* 8 (2018) 1702582.
- [8] B. Cao, Q. Zhang, H. Liu, B. Xu, S. Zhang, T. Zhou, J. Mao, W.K. Pang, Z. Guo, A. Li, J. Zhou, X. Chen, H. Song, *Adv. Energy Mater.* 8 (2018) 1801149.
- [9] Y. Yang, Y. Tang, G. Fang, L. Shan, J. Guo, W. Zhang, C. Wang, L. Wang, J. Zhou, S. Liang, *Energy Environ. Sci.* 11 (2018) 3157–3162.
- [10] F. Wang, O. Borodin, T. Gao, X. Fan, W. Sun, F. Han, A. Faraone, J.A. Dura, K. Xu, C. Wang, *Nat. Mater.* 17 (2018) 543–549.
- [11] C. Xia, J. Guo, Y. Lei, H. Liang, C. Zhao, H.N. Alshareef, *Adv. Mater.* 30 (2018) 1–7.
- [12] M. Yu, Y. Lu, H. Zheng, X. Lu, *Chem. - A Eur. J.* 24 (2018) 3639–3649.
- [13] N. Zhang, F. Cheng, J. Liu, L. Wang, X. Long, X. Liu, F. Li, J. Chen, *Nat. Commun.* 8 (2017) 1–9.
- [14] L. Chen, J.L. Bao, X. Dong, D.G. Truhlar, Y. Wang, C. Wang, Y. Xia, *ACS Energy Lett.* 2 (2017) 1115–1121.
- [15] D. Kundu, B.D. Adams, V. Duffort, S.H. Vajargah, L.F. Nazar, *Nat. Energy* 1 (2016) 1–8.
- [16] M. Adil, P.K. Dutta, S. Mitra, *ChemistrySelect* 3 (2018) 3687–3690.
- [17] J. Joseph, J. Nerkar, C. Tang, A. Du, A.P. O'Mullane, K. (Ken) Ostrikov, *ChemSusChem* 12 (2019) 1–9.
- [18] L. Chen, Z. Yang, J. Wu, H. Chen, J. Meng, *Electrochim. Acta* 330 (2019) 135347.
- [19] H. Li, C. Xu, C. Han, Y. Chen, C. Wei, B. Li, F. Kang, *J. Electrochem. Soc.* 162 (2015) A1439–A1444.
- [20] W. Qiu, Y. Li, A. You, Z. Zhang, G. Li, X. Lu, Y. Tong, *J. Mater. Chem. A* 5 (2017) 14838–14846.
- [21] T. Wei, Q. Li, G. Yang, C. Wang, *J. Mater. Chem. A* 6 (2018) 8006–8012.
- [22] L. Zhang, L. Chen, X. Zhou, Z. Liu, *Adv. Energy Mater.* 5 (2015) 1–5.
- [23] J. Li, K. McColl, X. Lu, S. Sathasivam, H. Dong, L. Kang, Z. Li, S. Zhao, A.G. Kafizas, R. Wang, D.J.L. Brett, P.R. Shearing, F. Corà, G. He, C.J. Carmalt, I.P. Parkin, *Adv. Energy Mater.* 2000058 (2020) 1–14.
- [24] X. Wang, F. Wang, L. Wang, M. Li, Y. Wang, B. Chen, Y. Zhu, L. Fu, L. Zha, L. Zhang, Y. Wu, W. Huang, *Adv. Mater.* 28 (2016) 4904–4911.
- [25] L. Ma, S. Chen, H. Li, Z. Ruan, Z. Tang, Z. Liu, Z. Wang, Y. Huang, Z. Pei, J.A. Zapien, C. Zhi, *Energy Environ. Sci.* 11 (2018) 2521–2530.
- [26] R. Zhang, C. Pan, R.G. Nuzzo, A.A. Gewirth, *J. Phys. Chem. C* 123 (2019) 8740–8745.
- [27] L. Yin, Z. Zhang, Z. Li, F. Hao, Q. Li, C. Wang, R. Fan, Y. Qi, *Adv. Funct. Mater.* 24 (2014) 4176–4185.
- [28] W. Shang, W. Yu, P. Tan, B. Chen, H. Xu, M. Ni, *J. Power Sources* 421 (2019) 6–13.
- [29] Z.Q. Liu, H. Cheng, N. Li, T.Y. Ma, Y.Z. Su, *Adv. Mater.* 28 (2016) 3777–3784.

- [30] J. Zhu, D. Song, T. Pu, J. Li, B. Huang, W. Wang, C. Zhao, L. Xie, L. Chen, *Chem. Eng. J.* 336 (2018) 679–689.
- [31] W. Luo, X. Hu, Y. Sun, Y. Huang, *J. Mater. Chem.* 22 (2012) 8916–8921.
- [32] C. Pan, R.G. Nuzzo, A.A. Gewirth, *Chem. Mater.* 29 (2017) 9351–9359.
- [33] C.H. Chu, C.W. Leung, *Integr. Equations Oper. Theory* 40 (2001) 391–402.
- [34] A.Z. AlZahrani, *ISRN Condens. Matter Phys.* 2012 (2012) 1–8.
- [35] G. Kresse, J. Furthmüller, *Comput. Mater. Sci.* 6 (1996) 15–50.
- [36] G. Kresse, J. Hafner, *Phys. Rev. B* 49 (1994) 14251–14269.
- [37] P.E. Blöchl, *Phys. Rev. B* 50 (1994) 17953–17979.
- [38] J.P. Perdew, K. Burke, M. Ernzerhof, *Phys. Rev. Lett.* 77 (1996) 3865–3868.
- [39] H.J.M. James D. Pack, *J. Chem. Inf. Model.* 16 (1977) 1748–1749.
- [40] Z. Cai, Y. Bi, E. Hu, W. Liu, N. Dwarica, Y. Tian, X. Li, Y. Kuang, Y. Li, X.Q. Yang, H. Wang, X. Sun, *Adv. Energy Mater.* 8 (2018) 1–8.
- [41] Y. Zeng, Z. Lai, Y. Han, H. Zhang, S. Xie, X. Lu, *Adv. Mater.* 30 (2018) 1–8.
- [42] H. Chen, X. Du, J. Sun, H. Mao, R. Wu, C. Xu, *Appl. Surf. Sci.* 515 (2020) 146008.
- [43] Q. Zhang, C. Li, Q. Li, Z. Pan, J. Sun, Z. Zhou, B. He, P. Man, L. Xie, L. Kang, X. Wang, J. Yang, T. Zhang, P.P. Shum, Q. Li, Y. Yao, L. Wei, *Nano Lett.* 19 (2019) 4035–4042.
- [44] G. He, M. Qiao, W. Li, Y. Lu, T. Zhao, R. Zou, B. Li, J.A. Darr, J. Hu, M.M. Titirici, I.P. Parkin, *Adv. Sci.* 4 (2017) 1600214.
- [45] L. Zhang, L. Chen, X. Zhou, Z. Liu, *Adv. Energy Mater.* 5 (2015) 1–5.
- [46] P. Hu, T. Wang, J. Zhao, C. Zhang, J. Ma, H. Du, X. Wang, G. Cui, *ACS Appl. Mater. Interfaces* 7 (2015) 26396–26399.
- [47] K. Lu, B. Song, J. Zhang, H. Ma, *J. Power Sources* 321 (2016) 257–263.
- [48] K. Lu, B. Song, Y. Zhang, H. Ma, J. Zhang, *J. Mater. Chem. A* 5 (2017) 23628–23633.
- [49] G. Li, Z. Yang, Y. Jiang, W. Zhang, Y. Huang, *J. Power Sources* 308 (2016) 52–57.
- [50] R. Trócoli, F. La, *ChemSusChem* 8 (2015) 481.
- [51] I.L. Santana, T.F.M. Moreira, M.F.F. Lelis, M.B.J.G. Freitas, *Mater. Chem. Phys.* 190 (2017) 38–44.
- [52] H. Zhang, J. Wang, Q. Liu, W. He, Z. Lai, X. Zhang, M. Yu, Y. Tong, X. Lu, *Energy Storage Mater.* 21 (2019) 154–161.
- [53] S. Gu, C. Hsieh, *J. Solid State Elec.* 23 (2019) 1399–1407.
- [54] Z. Zhao, J. Yao, B. Sun, S. Zhong, X. Lei, B. Xu, *Solid State Ionics* 326 (2018) 145–149.
- [55] Y. Lu, J. Wang, S. Zeng, L. Zhou, W. Xu, D. Zheng, J. Liu, Y. Zeng, X. Lu, *J. Mater. Chem. A* 7 (2019) 21678–21683.

Graphical Abstract

A unique 3D flower-like zinc cobaltite ($\text{ZnCo}_2\text{O}_{4-x}$) with oxygen vacancies is designed and fabricated and a flexible solid-state ZIB was demonstrated, which delivers an extremely stable capacity under bending states.

